Lewis number effect in lean premixed H_2-air and CH_4-air flames during thermoacoustic instability in a low-swirl combustor

Judai Masugi,[1,*] Takeshi Shoji,[2] Yoshihiro Nakazumi,[1] Ryota Fujii,[1] Takuya Tomidokoro,[3] Shigeru Tachibana,[2] and Takeshi Yokomori[4,†]

[1]*Keio University, Graduate School of Science and Technology, 3-14-1 Hiyoshi, Kohoku-ku, Yokohama, Kanagawa 223–8522, Japan*

[2]*Japan Aerospace Exploration Agency, Aviation Technology Directorate, 7-44-1 Jindaiji Higashi-machi, Chofu, Tokyo 182–8522, Japan*

[3]*King Abdullah University of Science and Technology, CCRC, PSE Division, 4700 King Abdullah University of Science and Technology, Thuwal 23955–6900, Kingdom of Saudi Arabia*

[4]*Keio University, Department of Mechanical Engineering, 3-14-1 Hiyoshi, Kohoku-ku, Yokohama, Kanagawa 223–8522, Japan*

(Received 3 December 2023; accepted 20 December 2024; published 21 April 2025)

Suppression of NO_x and CO_2 emissions in gas turbines is an urgent challenge. While lean premixed combustion is a strategy for reducing NO_x production, the occurrence of thermoacoustic instability is a significant issue. In addition, while hydrogen is a promising fuel for replacing conventional hydrocarbon fuels and reducing CO_2 emissions, the unsteady flame-flow dynamics of hydrogen flames under thermoacoustic instabilities remain to be elucidated. Recently, low-swirl combustors have attracted attention since they can stabilize flames with a wide range of fuel compositions including pure hydrogen-air flames. In particular, the characteristics of hydrogen flames are expected to be significantly influenced by its Lewis number Le, where it is $\mathrm{Le} < 1$ for hydrogen-air flames in contrast to $\mathrm{Le} \approx 1$ for methane-air flames. Therefore, this study experimentally analyzes the Lewis number effect in hydrogen and methane flames during thermoacoustic instability and discuss its influence on the local flame-flow interactions. The flames were stabilized in a low-swirl combustor with a geometric swirl number of 0.39. Pressure fluctuation measurements, OH* chemiluminescence imaging, and particle imaging velocimetry were performed simultaneously. It was found that the pressure fluctuation amplitude was nearly three times larger in the hydrogen flame than in the methane flame. To discuss the Lewis number effect, the instantaneous flame stretch rate and the chemiluminescence intensity were calculated at the local flame tip along the center axis. This analysis revealed that in the hydrogen flame ($\mathrm{Le} < 1$), the flame stretch rate fluctuation strongly correlated with the chemiluminescence intensity fluctuation, while the correlation between those in the methane flame ($\mathrm{Le} \approx 1$) was found to be weaker. Therefore, it was concluded that, in the hydrogen flame, the Lewis number effect is responsible for the coupling between the heat release rate fluctuation and the flow fluctuation at the local flame tip during thermoacoustic instability.

DOI: 10.1103/PhysRevFluids.10.043201

*Contact author: j.masugi2828@keio.jp
†Contact author: yokomori@mech.keio.ac.jp

 ©2025 American Physical Society

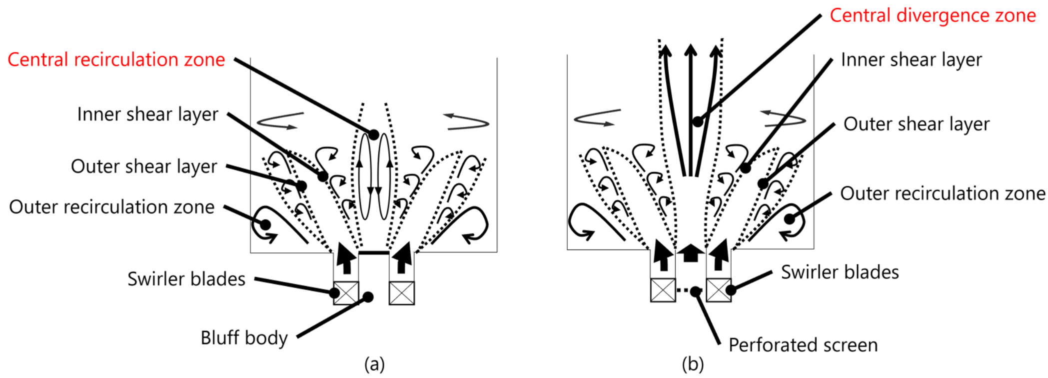

FIG. 1. General flow field formed in (a) a HSC, (b) a LSC.

I. INTRODUCTION

Low-emission technologies are required in gas turbines, which are widely used for propulsion and power generation. Specifically, suppression of NO_x emissions from the combustion process has long been a central issue. An effective way to reduce NOx emissions is to lower the flame temperature by introducing lean premixed combustion systems [1]. However, since lean premixed flames are unstable, combustion instability, blowoff, and flashback have been significant issues [2–4]. In particular, combustion instability induces large pressure oscillations that can critically damage the combustor and other structural components. It is generally understood that the thermoacoustic instability is driven and amplified by the feedback loop involving pressure fluctuations in the combustor chamber, the heat release rate fluctuation of the flame, and the fluctuation in the flow field [5]. However, the details of this feedback process are still extensively studied [6–9].

Meanwhile, eliminating CO_2 emissions from combustion is another urgent challenge. To replace conventional hydrocarbon-based fuels, hydrogen has attracted global attention as a carbon-free alternative fuel. Here, lean premixed combustion is effective not only for suppressing thermal NO_x emissions, but also for reducing the high burning velocity of hydrogen flames. Therefore, many studies have been performed to address the thermoacoustic instabilities during lean premixed combustion of hydrogen fuels [10–12].

Numerous studies have explored the impact of the hydrogen enrichment in hydrocarbon fuels such as methane and have reported differences in thermoacoustic instability characteristics in high-swirl combustors [13–18], bluff-body burners [19], and annular combustors [20]. It has been reported that the hydrogen enrichment of methane flames may result in modification of the flame structure [13,15,16,19] and pressure oscillation characteristics [15–20]. In particular, different studies [17,18] have reported that hydrogen enrichment can either suppress or amplify the thermoacoustic instability. Therefore, further studies are required to fully elucidate the impact of hydrogen enrichment.

Many of the above studies have targeted a high-swirl combustor (HSC). A HSC is a typical configuration used in modern gas turbines; it consists of a center bluff body surrounded by swirl blades. The formation of the central recirculation zone downstream of the bluff body, as Fig. 1(a) shows, is critical to the stabilization of the flame in a HSC. In a HSC, the flashback event due to the combustion-induced vortex breakdown is crucial. It has been noted that flashback can occur at low equivalence ratios with the use of fuels with high hydrogen compositions compared to methane flames [21]. Therefore, a weak point of a HSC is that pure hydrogen flames can only be stabilized for a narrow range of equivalence ratios.

Conversely, a low-swirl combustor (LSC) can stabilize flames across wide ranges of equivalence ratios and fuel compositions, including pure hydrogen. The first LSC was developed by Lawrence Berkeley National Laboratory in 1992 to study the interaction between turbulent flows and flames in a model gas turbine [22]. Today, LSCs are already being used in gas turbine power generators [10,23]. Figure 1(b) shows the general flow field formed in a LSC. Replacing the central bluff body with a perforated plate featuring a nonswirling flow inhibits the vortex breakdown and creates a central divergence zone. Therefore, the flame self-sustains when the flame displacement speed balances with the bulk flow velocity at the center axis of the combustor.

Thermoacoustic instabilities in LSCs have been studied from the aspect of introducing inhomogeneous fuel injection [24] and multistage swirlers [25] and the use of hydrogen fuels [12,26,27]. In particular, Yilmaz *et al*. [26] and Therkelsen *et al*. [27] reported differences in the thermoacoustic instability characteristics between a hydrocarbon flame and a hydrogen-enriched methane flame. Yilmaz *et al*. [26] focused on the Rayleigh index analysis. They examined the acoustic-induced thermoacoustic instability in various hydrogen-enriched methane/air flames. Their results showed that the value of the Rayleigh index in the vicinity of the flame base transfers to positive under typical hydrogen compositions. Their study assumed that hydrogen enrichment made the flame sensitive, but no further discussion appeared in their report. Therkelsen *et al*. [27] investigated in the flame-vortex interaction and the flame configuration. They observed the self-excited thermoacoustic instability in a methane-air flame and a 90% hydrogen/10% methane-air flame. They applied a laser beam deflection method to examine flames's responses to the pressure oscillation. A common response between two fuel compositions was that both flames fluctuated at the same frequency as the pressure oscillated in the outer regions of each flame. However, they found a difference in the vicinity of the flame base along the center axis. The methane flame did not react to the pressure oscillation, whereas the hydrogen flame fluctuated at the same frequency as the pressure oscillation. Those authors indicated that there is a stronger interaction between the flow and the hydrogen flame than between the flow and the methane flame. However, due to a lack of measurements, the details were not explained, and the heat release rate fluctuations could not be addressed. While it was implied that hydrogen enrichment made the flame more sensitive to the flow fluctuation [26,27], no further discussion on its physical mechanism appeared in their report.

So far, few studies [28,29] have investigated the roles of the Lewis number Le during the thermoacoustic instability. Le is defined as the ratio of thermal diffusivity α to mass diffusivity D_{def} of the deficient species in the premixture [30]. In a flame that is stretched by the flow, the combustion strength varies according to the Lewis number and the flame stretch rate. This is called the Lewis number effect [30–34]. Since the general Lewis number of the lean hydrogen-air premixture is $\mathrm{Le} < 1$, the hydrogen flame is expected to be sensitive to fluctuations in the flow field. Yoon *et al*. [29] experimentally compared the strength of the acoustic sound of the thermoacoustic instability in premix gases composed of ethylene, oxygen, carbon dioxide, and nitrogen with various Lewis numbers. The results showed that the $\mathrm{Le} < 1$ flame had the largest pressure amplitude in the study. However, studies on the local effect of the Lewis number on hydrogen flames during thermoacoustic instability are limited.

As such, the present study aims to experimentally investigate the Lewis number effect on the local flame-flow interaction during thermoacoustic instability. To achieve this, hydrogen ($\mathrm{Le} < 1$) and methane ($\mathrm{Le} \approx 1$) flames stabilized in a LSC were compared. The current analysis focused on the vicinity of the flame tip along the center axis of the combustor. This is the region where the flame is anchored in a LSC, and the local correlation between the flame and the flow fluctuation can be interpreted straightforwardly (see details in Sec. III B 2). Meanwhile, investigation of the influence of such a local flame-flow interaction on the global thermoacoustic instability is out of scope of the current objective and left for future studies.

II. EXPERIMENTAL CONFIGURATION

A. Low-swirl combustor

Figure 2 shows a schematic of the LSC and the fuel-air supply system. The coordinate axes are also defined in the figure. The fuel, whether hydrogen or methane, was fully mixed with the

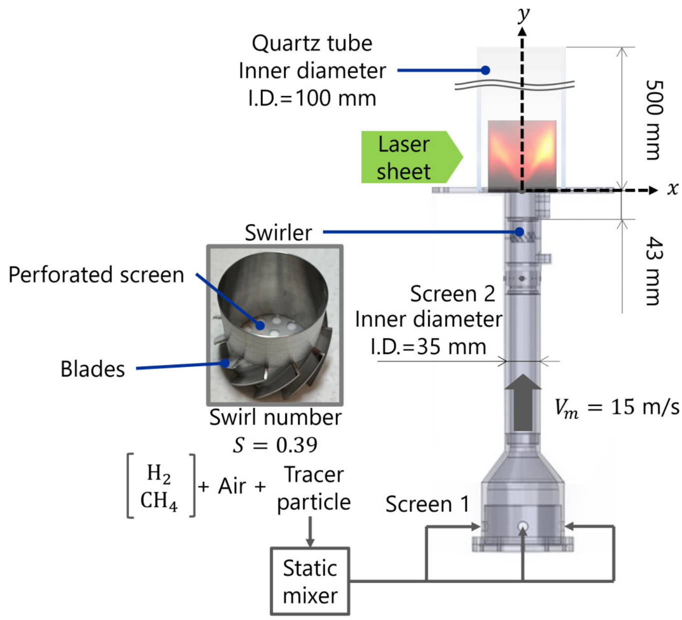

FIG. 2. Schematic of the LSC (side view).

compressed air in a static mixer and was supplied to the LSC from four directions. The premixed gas passed through two screens to reach the swirler, the top of which was placed 43 mm upstream of the dump plane ($y = 0$ mm). The inner diameter D of the nozzle of the LSC was 35 mm. The swirler consisted of 12 blades inclined 37° to the axial direction and a perforated screen with 19 holes (3.6 mm in diameter). The geometric swirl number $S_w = 0.39$ was calculated based on Ref. [35],

$$S_w = \frac{2}{3}\tan\alpha_{\text{blade}}\frac{1 - R^3}{1 - R^2 + [m^2(1/R^2 - 1)^2]R^2}, \tag{1}$$

where, α_{blade} is the inclined angle of blades, R is the radius ratio between the perforated screen and the swirler, and m is the mass flux ratio. A quartz tube with a length of 500 mm and an inner diameter of 100 mm was located at the nozzle exit, enabling the combustion chamber to be optically accessed. In this study, the bulk flow velocity V_m and geometric parameters (the size of the quartz tube and swirl number S_w) were fixed for all conditions.

B. Simultaneous measurement systems

Figure 3 shows a schematic of the measurement system. The coordinates are shown in the figure, with $(x, y, z) = (0, 0, 0)$ mm defined as the center of the combustor nozzle and the height of the face plate. However, the coordinate symbol is shifted for visibility.

The pressure fluctuation p' in the combustion chamber was measured at $(x, y, z) = (0, 0, 35)$ mm using a water-cooled pressure transducer (Kulite, WCT-312–5SG) at a sampling rate of 200 kHz.

OH* chemiluminescence, which is known to be related to the heat release rate [36] was recorded by a high-speed camera (Photron, SA-X2) at 10 kHz. An image intensifier (Lambert, HiCATT 25D), a 100 mm UV lens (Sodern, CERCO 2178) at f/2.8, a band-pass filter to extract 308 nm OH* chemiluminescence, and a short-pass filter to remove 532 nm laser light for PIV were mounted to the high-speed camera. The field of view was approximately $-50 < x < 50$ mm, $0 < y < 100$ mm

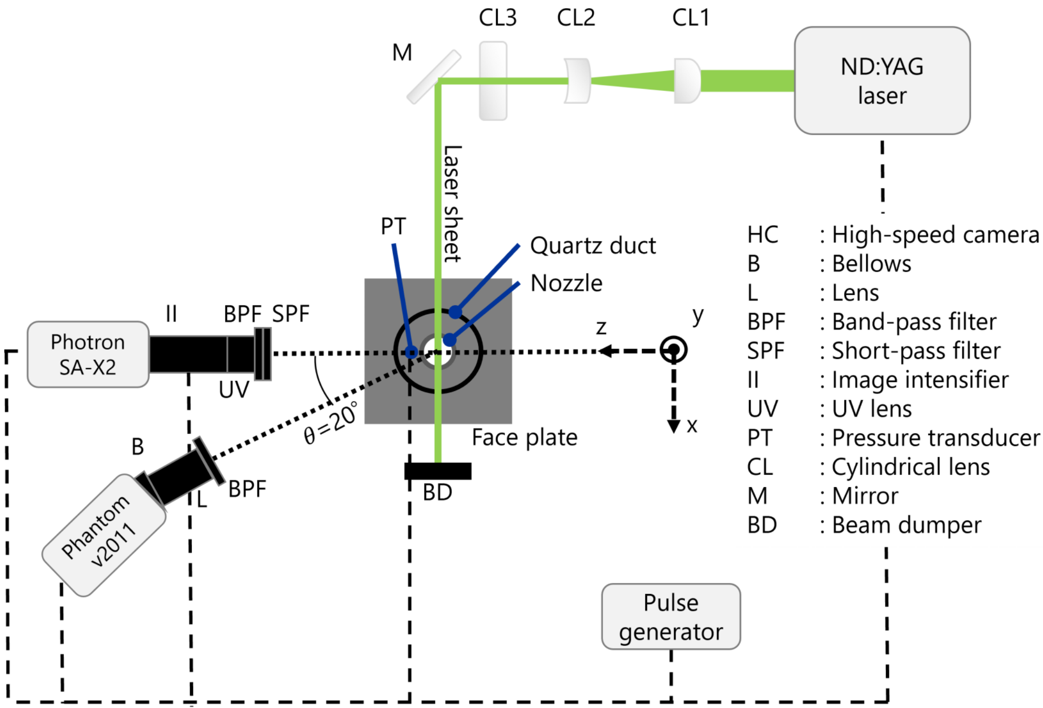

FIG. 3. Schematic of the measurement system (top view).

square, and the spatial resolution was 0.114 mm/pixel for the hydrogen flame and 0.112 mm/pixel for the methane flame. A total of 5000 images were taken.

Particle imaging velocimetry (PIV) was conducted to measure the velocity field by utilizing a high-speed camera (Phantom v2011) at 40 kHz. The camera settings were based on the Scheimpflug condition [37]. A 200 mm lens (Nikon AF MICRO NIKKOR) at f/4.0 and a band-pass filter to extract 532 nm laser light were mounted to the high-speed camera. A laser sheet (3.5 mm thick, 80–90 mm high) was formed with a 532 nm laser beam generated by an Nd: YAG laser (EdgeWave GX600-2-L) and irradiated onto the x-y plane. Tracer particles (SiO_2, 2.7 μm in diameter) were mixed into the premixed flow using a static mixer, and the camera recorded their Mie scattering. The field of view was $-50 < x < 20$ mm, $0 < y < 60$ mm and the spatial resolution was 0.0962 mm/pixel. The final window size was 16 pixels, and the vector spacing was 0.770 mm. A total of 20000 images were taken. These conditions were applied to both the hydrogen and methane flame.

C. Experimental conditions

Pressure fluctuations were first measured as a primary test (see Sec. III A for details) to determine the equivalence ratio in which the largest pressure amplitude was observed. According to the results of the preliminary test, simultaneous measurements were performed at an equivalence ratio of $\phi = 0.28$ (Le $= 0.34$) for the hydrogen flame and $\phi = 0.62$ (Le $= 0.97$) for the methane flame.

The laminar flame speed and the Lewis number for each premixture was calculated as follows. The premixed laminar flame speed calculation was conducted using ANSYS 2019 R3 Chemkin-Pro (GRI-Mech 3.0 mechanism). Inlet conditions were defined as ambient temperature (300 K) and pressure (1 atm). The laminar flame speed is defined as the inlet velocity that allows the flame to stay in a fixed position. To calculate the Lewis number, unburned gas quantities, which are thermal conductivity λ, heat capacity C_p, mass density ρ, and mass diffusivity D_{def}, were evaluated at the

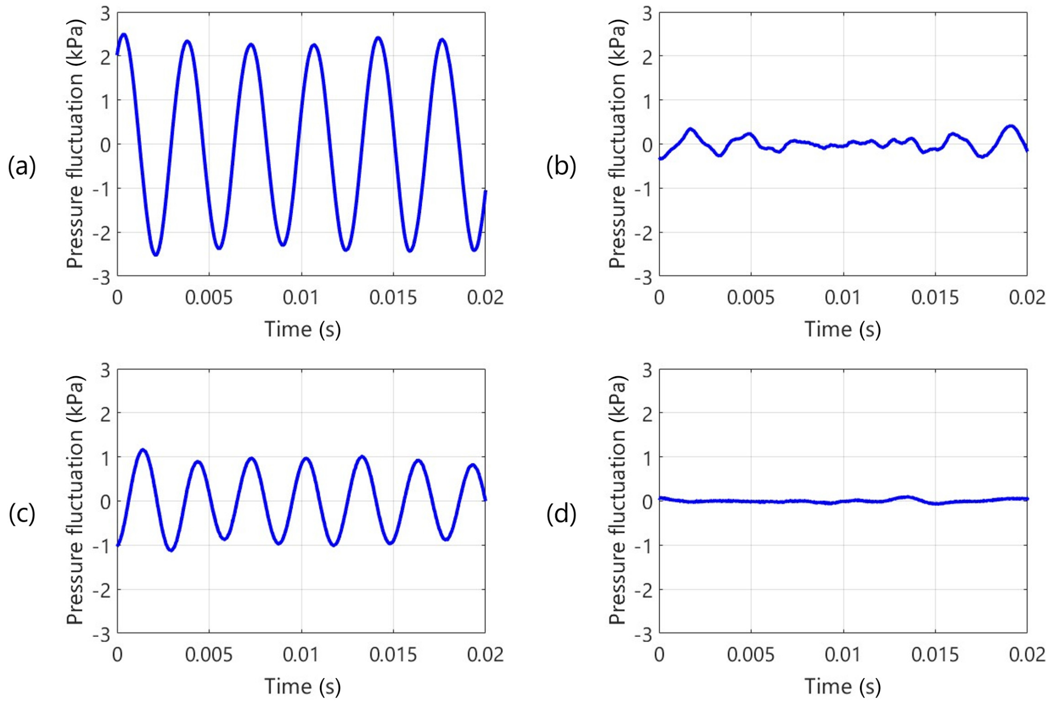

FIG. 4. Time series of pressure fluctuation measurements for (a) the thermoacoustic instability case; hydrogen flame, $\phi = 0.28$, (b) the stable case; hydrogen flame, $\phi = 0.34$, (c) the thermoacoustic instability case; methane flame, $\phi = 0.62$, (d) the stable case; methane flame, $\phi = 0.56$.

inlet boundary. Here, the temperature and species concentration profiles had nearly zero gradient near both inlet and outlet boundaries. The Lewis number of the unburned premixture was then calculated as $\mathrm{Le} = (\lambda/\rho C_p)/D_{\mathrm{def}}$.

Fuel and compressed air volumetric flow rates were controlled using mass flow controllers, resulting in a total volumetric flow rate of approximately 866 L/min, corresponding to $V_m =$ 15 m/s at the combustor nozzle exit ($y = 0$ mm).

III. RESULTS AND DISCUSSIONS

A. Pressure fluctuation p' measurement

Pressure fluctuations were measured primarily for hydrogen flames in the range of $0.20 < \phi < 0.40$ (with a 0.02 interval) and methane flames in the range of $0.56 < \phi < 0.76$ (with a 0.02 interval).

First, Fig. 4 shows a partial time series of pressure fluctuation measurements. In the case of the thermoacoustic instability [Figs. 4(a) and 4(c)], noticeable pressure fluctuations were observed compared to the stable case [Fig. 4(b) and 4(d)] for both flames. Also, the instantaneous pressure amplitude was approximately twice as large in the hydrogen flame than in the methane flame in the thermoacoustic instability case.

Second, pressure fluctuation p' spectra for both flames are shown in Fig. 5. The peak frequency f_p of pressure fluctuations, measured in hertz (Hz), was determined using the power spectral density estimation method applied to acquired 5-sec records. The frequency resolution was 5 Hz. When increasing the equivalence ratio, both the pressure amplitude and the dominant frequency increased, reaching the largest pressure amplitude at a specific point. With a further increase in the equivalence

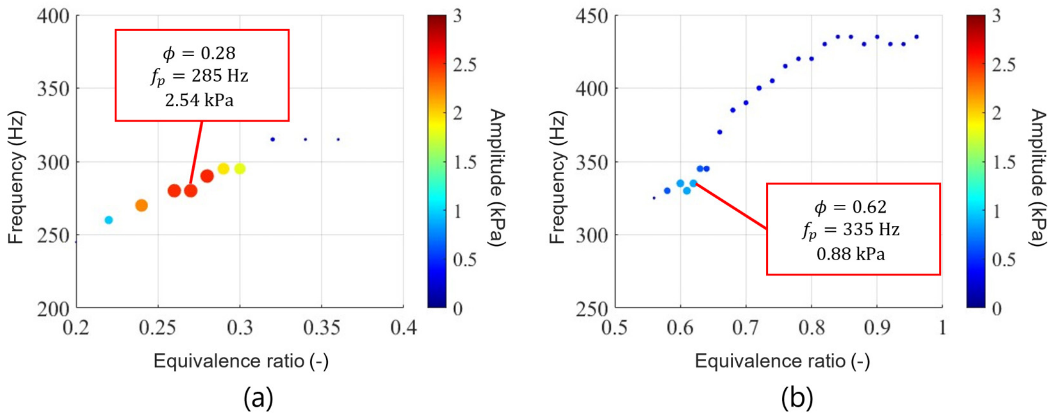

FIG. 5. The pressure fluctuation spectra p' for (a) hydrogen flames, (b) methane flames. The data points indicated by the red lines correspond to the conditions where the largest pressure fluctuation amplitude was observed for each fuel.

ratio, the pressure amplitude gradually decreased while the dominant frequency kept increasing. These trends aligned with the findings of several previous studies [15,38–40].

For further discussion, the equivalence ratio, which resulted in the maximum pressure amplitude, was selected for each flame, as shown in the red lines in Fig. 5. For the hydrogen flame, the maximum amplitude of 2.54 kPa at 285 Hz was observed when $\phi = 0.28$. For the methane flame, the maximum amplitude of 0.88 kPa at 335 Hz was observed at $\phi = 0.62$. It is intriguing to observe that, despite the same geometry, the maximum pressure amplitude for the hydrogen flame was nearly three times greater than that for the methane flame.

Note that the laminar flame speed S_L is different for above two cases. According to Fig. 5, for hydrogen flames, the pressure fluctuation is significant under $0.22 < \phi < 0.30$, and the corresponding laminar flame speed is approximately $3.5 < S_L < 5$ cm/s. Meanwhile, for methane flames, the pressure fluctuation is significant under $0.54 < \phi < 0.63$, and the corresponding laminar flame speed is approximately $8 < S_L < 15$ cm/s. Therefore, it would not be possible to observe the thermoacoustic instability under the same laminar flame speed. Since the objective of this study is to examine the Lewis number effect on local flame-flow interaction during the thermoacoustic instability, it was desirable to select conditions where significant pressure fluctuation was observed, rather than selecting conditions to achieve the same flame speed.

B. Results of PIV

1. Flame front estimation: Number density method

In this study, the local flame front (i.e., the upstream edge of the flame tip) formed in the vicinity of the center axis was estimated from instantaneous particle images captured for PIV, and the flame stretch rate κ was calculated. While OH* chemiluminescence images can also be used for estimating the flame front, it was deemed that using particle images would be more rigorous and better suited to the current analysis. There are two reasons for this decision. First, unlike the OH* chemiluminescence images, the PIV data is acquired in the *x*-*y* plane. Therefore, using particle images allows for accurate flame-front tracking and evaluation of the local strain rate (details in Sec. III B 2). In other words, the advantage of using particle images lies in the fact that flame quantities can be extracted on the same plane as the velocity field. Second, previous studies [41] have demonstrated methods to extract the flame front as the border between the sparse and dense regions of the particle number density, as will be explained below.

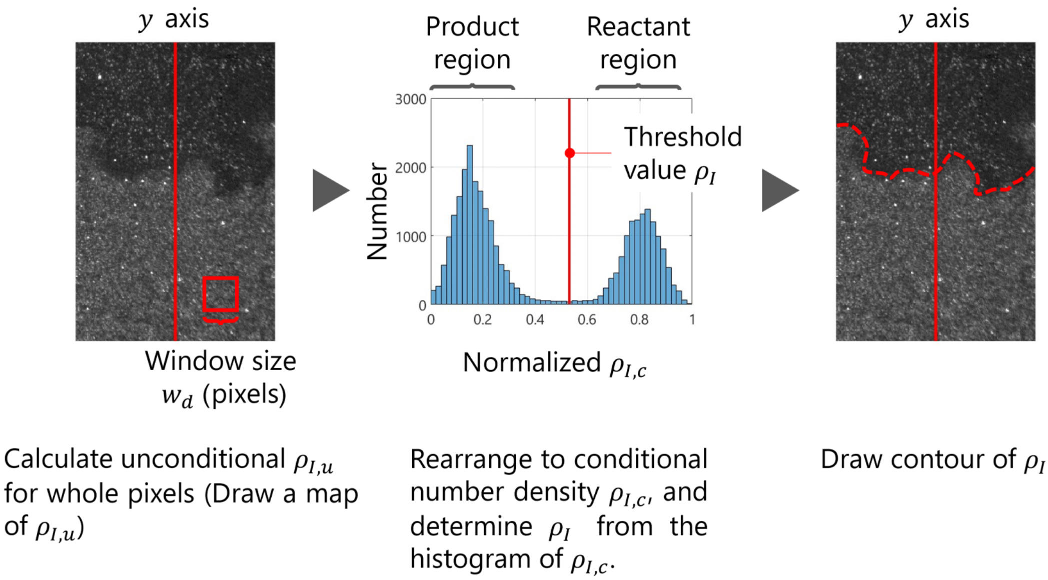

FIG. 6. Schematic of the number density method [37]. Particle images and histograms are the results acquired in this study.

In the combustion process, the number density of tracer particles decreases significantly in the flame zone as a result of thermal expansion in the flow. This results in a higher concentration of particles in the reactant region and a lower concentration in the product region. In the number density method, the border between the high and low particle concentration regions is defined as the flame front (i.e., the isothermal line). Figure 6 explains the procedure to estimate the flame front. To calculate the local number density at a given pixel, a square window of a certain size, denoted as w_d, is chosen. The unconditional number density $\rho_{I,u}$ is calculated as $\rho_{I,u} = N_I/w_d^2$, where N_I is the number of particles in the square window. $\rho_{I,u}$ is calculated for every pixel. Once $\rho_{I,u}$ is calculated for the entire region, the unconditional number density $\rho_{I,u}$ distribution map is generated as output. The results of $\rho_{I,u}$ are organized into a probability density function in the form of a histogram of $\rho_{I,u}$. In the histogram, two clear peaks are confirmed, which correspond to the reactant region for the peak at the high $\rho_{I,u}$ and the product region for the peak at the low $\rho_{I,u}$. The $\rho_{I,u}$ distribution map is then smoothed and recalculated as the conditional number density $\rho_{I,c}$ distribution map. Again, it is organized into a histogram as a PDF of conditional number density $\rho_{I,c}$. The minimum probability of $\rho_{I,c}$ that exists between two clear peaks corresponds to the threshold value ρ_I. The isocontour of ρ_I in $\rho_{I,c}$ distribution map expresses the estimated flame front, as shown in the far right of Fig. 6. Further details of the above procedure are explained in Ref. [41].

In the number density method, the window size w_d is a crucial parameter, as it directly influences the accuracy of the flame front position and the flame front curvature. A small window size causes a large deviation in the number density, which makes it difficult to separate the reactant and the product region. On the other hand, a large window size smoothes the data and results in the loss of information regarding the flame curvature. In this study, a window size of $w_d = 16$ pixels (1.54 mm) was used for both hydrogen and methane flames. An example of the estimated flame front during the thermoacoustic instability is depicted in the instantaneous raw particle image shown in Fig. 7. The red line indicates the center axis, while the blue line represents the estimated flame front. Note that while the seeding quality of the hydrogen flame was slightly poorer than that of the methane flame, it was sufficient to track the flame front. As described, the window size w_d directly affects the resolution of the number density distribution map, which, in turn, leads to the quality of the

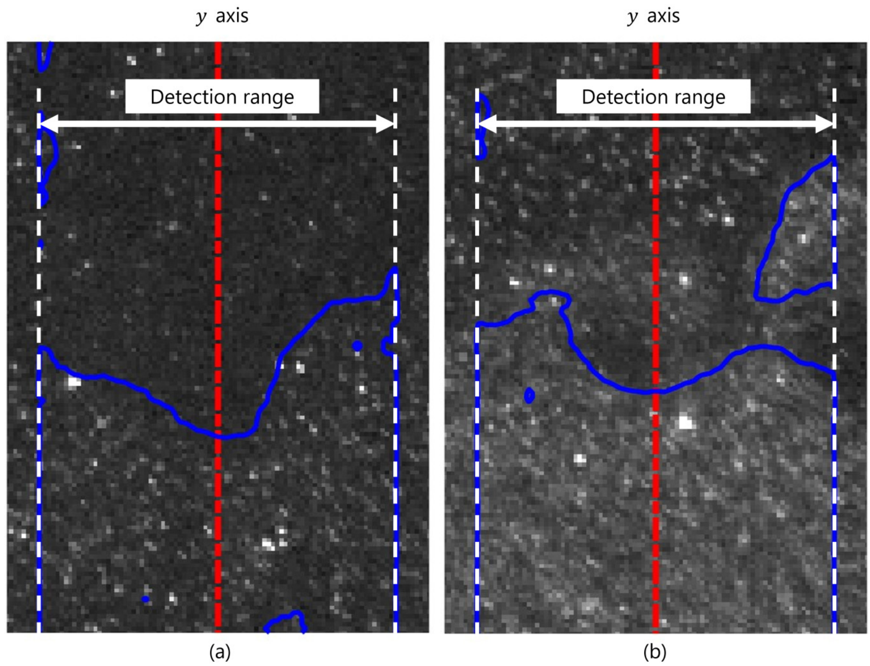

FIG. 7. Examples of the estimated flame front for (a) hydrogen flame; $t = 0.000600$ s, (b) methane flame; $t = 0.000850$ s. Blue lines indicate the isocontour of ρ_I in $\rho_{I,c}$ distribution map which corresponds to the estimated flame front.

curvature and the position of the flame front. In the following discussion, an evaluation was carried out to determine the appropriateness of the chosen window size.

An increase in window size results in a reduction in the local variance; however, smaller window sizes do not lead to a convergence of the average number density, as the nonuniformity of the particle distribution affects the number density measurement [41]. Figure 8 compares the averaged number density calculated using various window sizes, incremented by two pixels, in both the pure reactant and product regions. Each of the number density is calculated as unconditional number density $\rho_{I,u} = N_I/w_d^2$. A total of 100 images were used, and the error bars indicate the standard deviation. The results indicate a distinct separation in number density between the reactant region and the product region. It can be observed that, at the reactant region, the number density converges when the window size exceeds 16 in the hydrogen flame and 10 in the methane flame. At the product region, those sizes are 16 and 14, respectively. To ensure uniform accuracy, a window size of 16 was ultimately chosen for both flames. Figure 9 presents a comparison of the quality of the isocontour of the threshold value ρ_I, which corresponds to the estimated flame front along the center axis, determined from several window sizes: $w_d = 8,\ 16,\ 24$ pixels, corresponding to 0.770, 1.54, 2.31 mm for the hydrogen flame, and $w_d = 6,\ 16,\ 24$ pixels, corresponding to 0.577, 1.54, 2.31 mm for the methane flame, respectively. This indicates that the estimated flame front derived from a smaller window size ($w_d = 8$ pixels for the hydrogen flame, $w_d = 6$ pixels for the methane flame) exhibits roughness, while for a larger window size ($w_d = 24$ pixels for both the hydrogen flame and methane flame), it becomes overly smoothed, which does not accurately represent the details of the flame front. As a result, $w_d = 16$ pixels was selected.

Note that in Sec. III B 2, it was mentioned that the first term of Eq. (7) plays a dominant role in the flame stretch rate κ. This implies that the change in the value of the curvature has a relatively small effect. In total, 20000 instantaneous films were used to estimate the flame front for each flame.

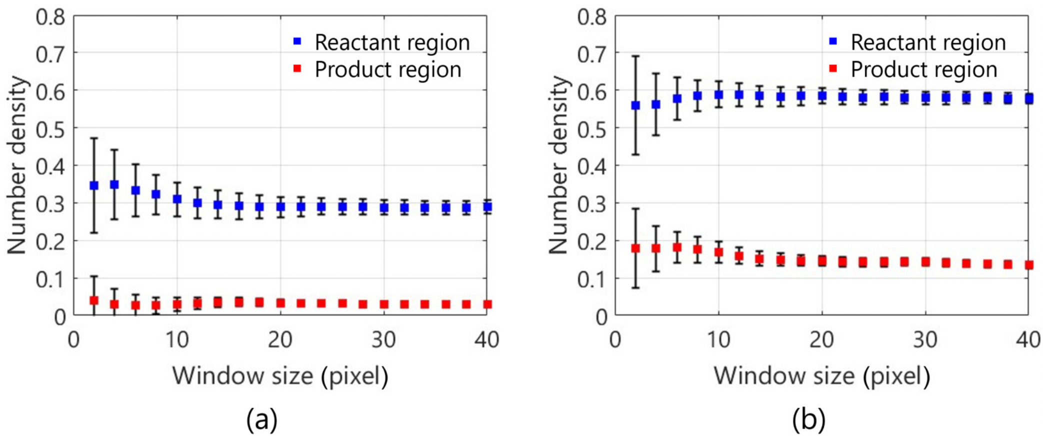

FIG. 8. The mean unconditional number density $\rho_{I,u} = N_I / w_d^2$ through 100 images in the pure reactant region and the pure product region for (a) hydrogen flame, (b) methane flame. Blue plot: The number density in the reactant region. Red plot: The number density in the product region. The error bar denotes the standard deviation.

2. Calculation of the flame stretch rate κ

After estimating the flame front, we proceeded to calculate the flame stretch rate, denoted as κ, along its length. The concept of the flame stretch rate κ was first suggested by Williams [42] and defined as Eq. (2) by Chung and Law [43] as

$$\kappa = -\{\nabla \times (\boldsymbol{V}_{\text{fluid}} \times \boldsymbol{n})\} \cdot \boldsymbol{n} + (\boldsymbol{v}_{\text{prop}} \cdot \boldsymbol{n})(\nabla \cdot \boldsymbol{n}), \tag{2}$$

where, $\boldsymbol{V}_{\text{fluid}}$ is the velocity of the fluid along the flame surface, $\boldsymbol{n}$ is the normal vector of the flame surface, and $\boldsymbol{v}_{\text{prop}}$ is the flame propagation speed. The first term generally represents the hydrodynamic strain along the flame surface, and the second term represents the influence of flame curvature and the flame displacement speed. In the present study, the flame stretch rate κ was calculated at the intersection point of the y axis and the estimated flame front.

Here, a coordinate for the flame (x', y', z') is defined. $(x', y', z') = (0, 0, 0)$ corresponds to the intersection point of the estimated flame front and the y axis. The x' axis corresponds to the tangential line and the y' axis corresponds to the normal line of the flame front.

When $\boldsymbol{n} = [0, 1, 0]$ and $\boldsymbol{V}_{\text{fluid}} = [u', v', w']$, the first term of Eq. (2) can be calculated as

$$-\{\nabla \times (\boldsymbol{V}_{\text{fluid}}) \times \boldsymbol{n}\} \cdot \boldsymbol{n} = \frac{\partial u'}{\partial x'} + \frac{\partial w'}{\partial z'}. \tag{3}$$

By assuming a quasisteady state, the continuity equation of incompressible fluid, $\partial u'/\partial x' + \partial v'/\partial y' + \partial w'/\partial z' = 0$, is substituted to Eq. (3). Then, the first term is transformed to

$$-\{\nabla \times (\boldsymbol{V}_{\text{fluid}} \times \boldsymbol{n})\} \cdot \boldsymbol{n} = -\frac{\partial v'}{\partial y'}. \tag{4}$$

To help the understanding, the mean x-y plane flow field is shown in Figs. 10(a) and 10(b). The field of view is approximately $-1.5 < x/D < 0.5$, $0 < y/D < 1.6$. Here, $D = 35$ mm is the combustor diameter. The measurement focused on the $x/D < 0$ region to achieve higher spatial resolution. While the data is missing around $x/D \approx -1.0$ due to reflection of the laser sheet, there is no influence on the current analysis. A typical LSC flow field, a swirling and large velocity flow in $-0.5 < x/D < -0.4$ and a small velocity flow in $-0.4 < x/D < 0.4$, was observed. The current analysis focuses on the region around the center axis, which is highlighted by the red box.

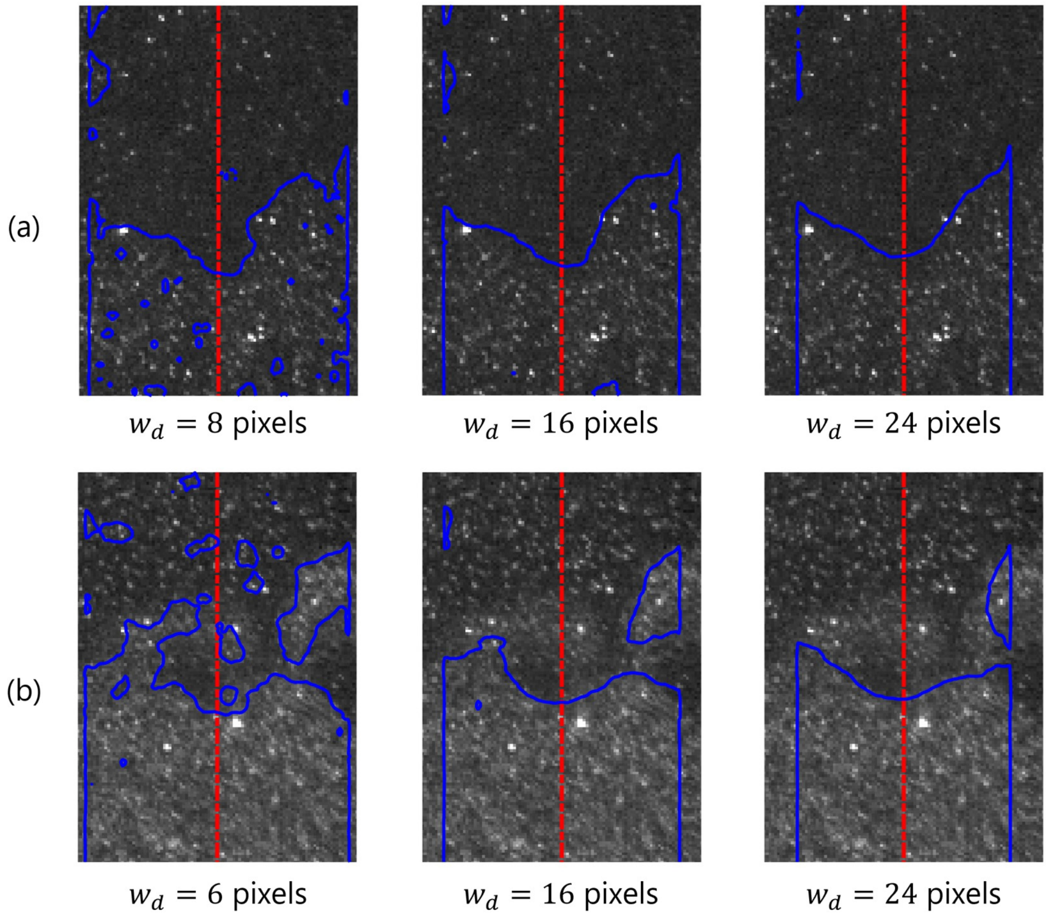

FIG. 9. Comparison of the flame front quality in various window sizes w_d for (a) hydrogen flame; $t = 0.000600$ s, (b) methane flame; $t = 0.000850$ s. Blue lines indicate the isocontour of ρ_I in $\rho_{I,c}$ distribution map, which corresponds to the estimated flame front. The straight line on both ends is not the flame front; they are ends for the detection range.

In a LSC, the flame that forms along the center axis has a deep bowl shape [27]. It is also known that the flow and the flame along the center axis intersect vertically [27,44]. Following these trends, both hydrogen and methane flames in this study predominantly exhibited a deep bowl shape even in the instantaneous flow field, as depicted in Figs. 10(c) and 10(d). Also, the relation between the flame and the flow mentioned in Ref. [44] is confirmed in Figs. 10(c) and 10(d). Therefore, the x-y axis and the x'-y' axis nearly matched. This situation led to the conclusion that calculating the first term of Eq. (2) along the laboratory coordinate $(x,\ y,\ z)$ was sufficient to describe the fluid dynamics along the flame front, allowing us to express the first term of Eq. (2) as

$$-\{\nabla \times (\boldsymbol{V}_{\text{fluid}} \times \boldsymbol{n})\} \cdot \boldsymbol{n} = -\frac{\partial v}{\partial y}. \tag{5}$$

Figure 11 illustrates the method to calculate $\partial v/\partial y$. Here is an example of the instantaneous vertical velocity profile along the center axis. Again, the vector spacing was 0.770 mm. Blue plots are the observed axial velocity along the center axis. Five velocity vectors upstream of the estimated flame front, which is shown in a black solid line in Fig. 11, were utilized to fit them into a linear function, reducing analytical noise. This resulted in a fitting range of 3.08 mm in width. Here, the

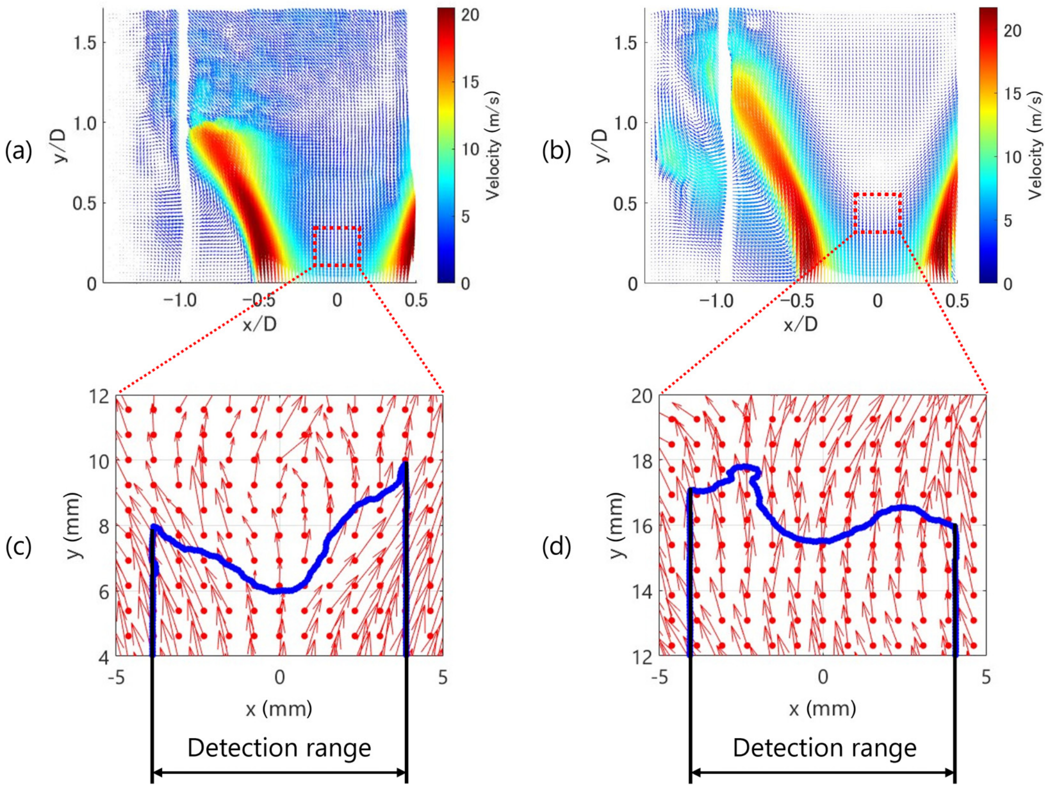

FIG. 10. The mean velocity field of (a) hydrogen flame, (b) methane flame. The field of view focused on the $x/D < 0$ side of the field. Data is missing around $x/D \approx -1.0$ because of the reflection of the laser. The red box corresponds to the area of (c) and (d). Examples of the instantaneous flame front and instantaneous flow field for (c) hydrogen flame, $t = 0.000600$ s, (d) methane flame, $t = 0.000850$ s. Red arrows show the velocity vector, and the blue line indicates the estimated flame front. The flame front exhibited a bowl shape. Also, the flow and the estimated flame front along the center axis intersect vertically. Note that (a) and (b) is a mean field, (c) and (d) is an instantaneous field.

fitting range was shifted upstream by a distance equal to the laminar flame thickness δ [mm]. This adjustment aimed to eliminate the influence of velocity increase caused by the thermal expansion and prevent the inclusion of velocity vectors within the flame zone. The laminar flame thickness was $\delta = 2.31$ mm for the hydrogen flame and $\delta = 0.924$ mm for the methane flame. δ was calculated as $\delta = (T_b - T_u)/(\mathrm{d}T/\mathrm{d}x)_{\max}$, where T_b indicates the burned temperature and T_u is the unburned temperature of the premixture. The temperature distribution was acquired from the results of the premixed laminar flame speed calculation, as explained in Sec. II C. Finally, the gradient of the linear fitting, shown by the red solid line in Fig. 11, was defined as $\partial v/\partial y$.

The second term of Eq. (2) was calculated as

$$(\boldsymbol{v}_{\mathrm{prop}} \cdot \boldsymbol{n})(\nabla \cdot \boldsymbol{n}) = S_L * \frac{\partial \boldsymbol{n}}{\partial x}, \tag{6}$$

where, S_L is the laminar flame speed and $\boldsymbol{n}$ is the normal vector of the flame front. $\partial \boldsymbol{n}/\partial x$ corresponds to the curvature R of the flame front. Again, the flame coordinate $(x',\ y',\ z')$ was assumed to match the laboratory coordinate (x, y, z). The flame displacement speed $\boldsymbol{v}_{\mathrm{prop}}$ was assumed to be the laminar flame speed S_L. This is because the resolution of the estimated flame front depends on the resolution of the particle image, which was 0.0962 mm. This is equivalent to the movement

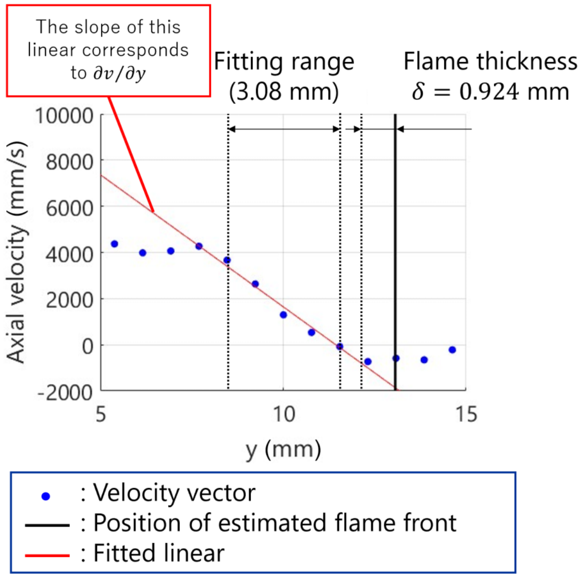

FIG. 11. Method of calculating $\partial v/\partial y$ (methane flame; $t = 0.385150$ s).

speed of 3.8 m/s between two adjacent images ($\Delta t = 0.000025$ s), which is unexpected and not characteristic of the flame displacement speed. The laminar flame speed S_L was calculated from the results of the premixed laminar flame speed calculation explained previously in Sec. II C. The laminar flame speed S_L was determined to be 3.97 cm/s for the hydrogen flame ($\phi = 0.28$), and 13.3 cm/s for the methane flame ($\phi = 0.62$). To calculate the curvature R, first, a quadric function $f_R(x)$ was fitted to the estimated flame front. The fitting range was the same as the calculation of κ, which is 3.08 mm. Second, $R = |f_R(x)''|/[1 + f_R(x)']^{\frac{3}{2}}$ was evaluated at $x = 0$. Here, $f_R(x)''$ and $f_R(x)'$ are the second-order and first-order differentials of $f_R(x)$, respectively.

Finally, κ was defined as

$$\kappa = -\frac{\partial v}{\partial y} + S_L * \frac{\partial \boldsymbol{n}}{\partial x}, \tag{7}$$

in this study. The conceptual scheme of Eq. (7) is illustrated in Fig. 12. Here, the y' axis was assumed to match the y axis, though $y' = 0$ originates to the intersection point of the estimated flame front and the y axis.

3. Phase-locked averaged flame stretch rate κ

A phase-locked averaging analysis [45] was performed to examine the periodic fluctuations occurring during the thermoacoustic instability. The peak frequency f_p [Hz] of the pressure fluctuation was evaluated by the power spectral density estimation method, as mentioned in Sec. III A, and a band-pass filter with a range of $f_p \pm 15$ Hz was applied. In this study, a phase angle of $\theta = 0^\circ$ was defined as the phase in which the maximum pressure fluctuation amplitude was observed. The phase resolution was set at 15°, resulting in 24 segments per cycle. This phase-locked average analysis was applied to evaluate the flame stretch rate κ as well as the vertical velocities at both the nozzle exit v_{nozzle} and the estimated flame front v_{flame}. In the present study, 20000 particle images were acquired. In the phase-locked averaging method, approximately 800 images were assigned to each phase.

First, the phase-locked averaged of the first term of the flame stretch rate κ (i.e., the strain rate), the phase-locked averaged curvature R, and the phase-locked averaged of the second term of the

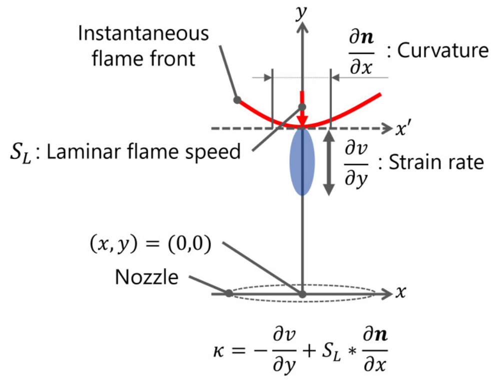

FIG. 12. Concept of calculation of $\kappa = -\frac{\partial v}{\partial y} + S_L * \frac{\partial \boldsymbol{n}}{\partial x}$.

flame stretch rate κ are represented in Fig. 13. The error bar denotes the standard deviation. Here, it is shown that the value of κ was dominated by the strain rate, which is the first term of κ, as shown in Figs. 13(a) and 13(b). Figures 13(e) and 13(f) showed that there were no clear periodic fluctuations in the second term of the flame stretch rate κ for either flame, and its value remained mostly under 10% of the first term. Also, according to Figs. 13(e) and 13(f), the second term in the methane flame is approximately three times larger than that in the hydrogen flame. This originates in the laminar flame speed S_L, which was 13.3 cm/s in the methane flame and 3.97 cm/s in the hydrogen flame. This also indicates that the magnitude of the curvature R value was equal for both flames, as shown in Figs. 13(c) and 13(d).

Second, Fig. 14 represents the phase-locked averaged flame stretch rate κ. Again, the error bar denotes the standard deviation. The mean value of κ and the fluctuation amplitude were different between the hydrogen flame and the methane flame. In the hydrogen flame, the mean value of κ was 253 /s and the amplitude was 275 /s; in the methane flame, those values were 356 /s and 104 /s. In other words, first, the mean value of κ in the methane flame is larger than the hydrogen flame, and second, the fluctuation amplitude of κ in the hydrogen flame is larger than in the methane flame. These trends can be explained by following the global flow characteristics.

Figures 15(b) and 15(c) indicate the phase-locked averaged axial velocity at the nozzle exit $[(x, y) = (0, 0)]$ v_{nozzle} and the flame front v_{flame}. Note that the data acquisition position of v_{nozzle} is fixed at the nozzle exit but varies for v_{flame} since the flame front moves. The schematic of the data acquisition point is illustrated in Fig. 15(a). As a common character shown in Figs. 15(b) and 15(c), the mean value and the fluctuation amplitude of v_{nozzle} are nearly equal for both hydrogen and methane flames. Meanwhile, a difference was observed in the trend of v_{flame}. Recall that in a LSC, the flame along the center axis stabilizes where the flame speed and the local flow velocity balance. Also, it is known that the axial velocity along the center axis decreases linearly in the reactant region [44]. Because of this mechanism, the faster the flame propagation speed is, the more the flame stabilizes close to the nozzle exit.]

In Figs. 15(b) and 15(c), the mean value of v_{flame} in the hydrogen flame is larger than in the methane flame. According to the above mechanism, this indicates that the lift-off height of the hydrogen flame is smaller than that of the methane flame. This also indicates that the hydrogen flame has a larger flame propagation speed than the methane flame. Such a difference in v_{flame} leads to the difference in the mean flame stretch rate κ observed in Fig. 14. In Figs. 15(b) and 15(c), $(v_{\text{nozzle}} - v_{\text{flame}})$ corresponds to the global velocity gradient between the nozzle exit and the flame front. It is seen that the value of $(v_{\text{nozzle}} - v_{\text{flame}})$ in the methane flame is larger than that of the hydrogen, which is the reason why the mean flame stretch rate κ of the methane flame is larger than that of the hydrogen flame. It is also confirmed that the difference in the lift-off height between the hydrogen flame and the methane flame has a small impact on the global velocity gradient.

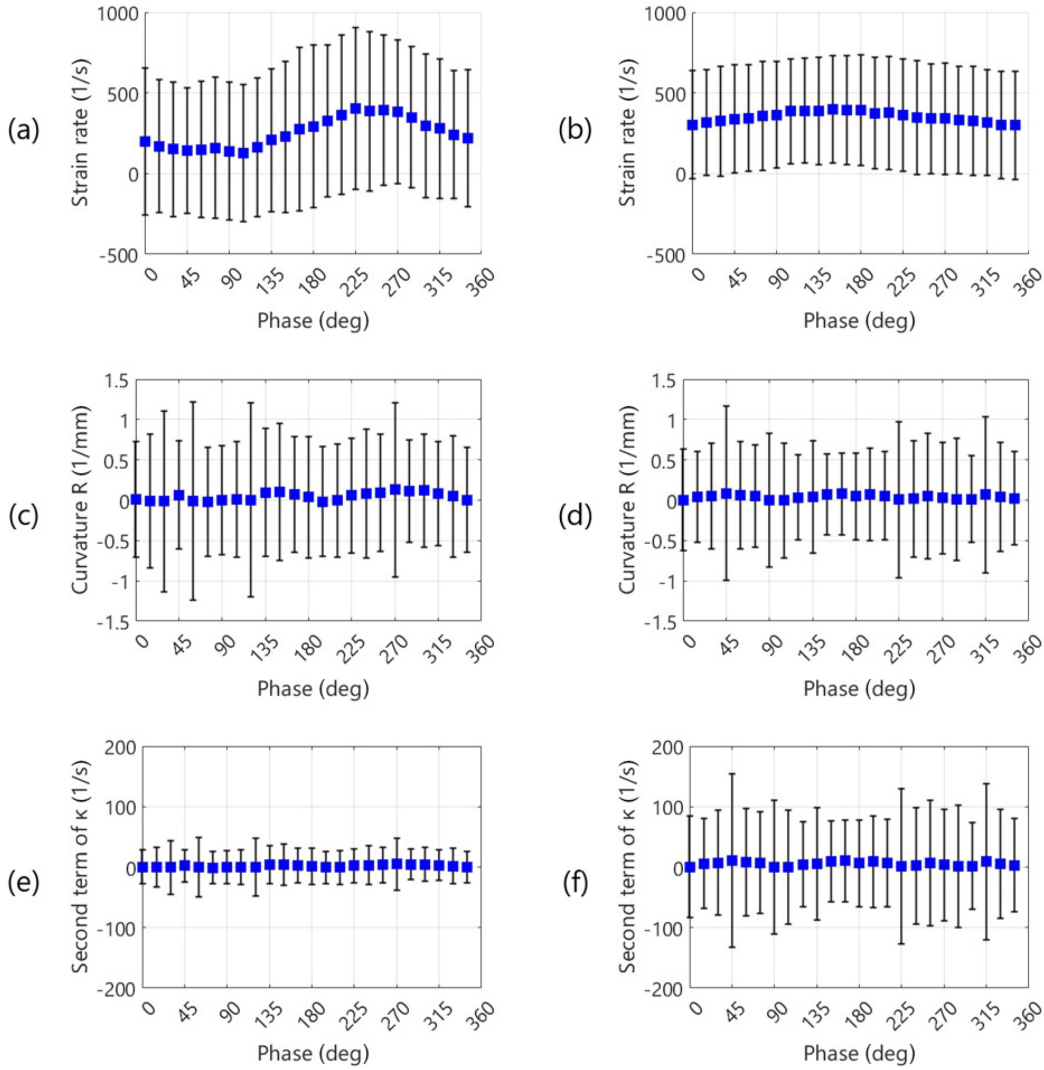

FIG. 13. The phase-locked average of the first term of the flame stretch rate κ for (a) hydrogen flame, (b) methane flame. The phase-locked averaged curvature R for (c) hydrogen flame, (d) methane flame. The phase-locked average of the second term of the flame stretch rate κ for (e) hydrogen flame, (f) methane flame. The phase $\theta = 0^\circ$ corresponds to the phase in which the maximum pressure fluctuation amplitude was observed.

The second trend; the difference in the fluctuation amplitude of the flame stretch rate κ, can also be explained by Figs. 15(b) and 15(c) in terms of the phase difference between $v_{\rm nozzle}$ and $v_{\rm flame}$. In the hydrogen flame, a phase difference of approximately 90 deg exists between $v_{\rm nozzle}$ and $v_{\rm flame}$. In the methane flame, on the other hand, there is nearly no phase difference. Due to the large phase difference in the hydrogen flame, the velocity gradient becomes large around $\theta = 225^\circ$ and small around $\theta = 75^\circ$, which led to a larger amplitude of the velocity gradient. On the other hand, in the methane flame, because the fluctuation amplitude of $v_{\rm flame}$ and the phase difference between $v_{\rm nozzle}$ and $v_{\rm flame}$ were small, the change in the velocity gradient mostly depended on the fluctuation of $v_{\rm nozzle}$. Accordingly, the fluctuation of the velocity gradient became smaller than the hydrogen flame.

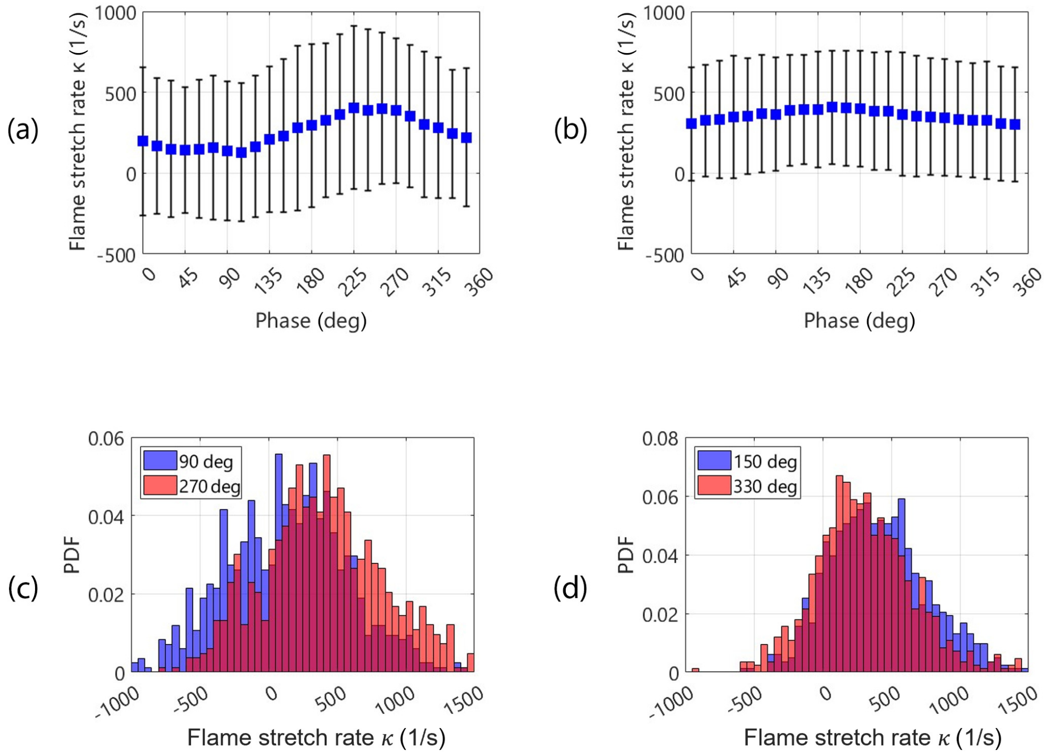

FIG. 14. The phase-locked averaged flame stretch rate κ for (a) hydrogen flame, (b) methane flame. PDF at the phase of minimum and maximum κ for (c) hydrogen flame, (d) methane flame. The phase $\theta = 0^\circ$ corresponds to the phases in which the maximum pressure fluctuation amplitude was observed.

Back to Fig. 14, in the hydrogen flame, a periodic fluctuation of κ was observed within the range of 129–404 /s. In the methane flame, κ also had a periodic fluctuation within the range of 303–407 /s. To further discuss the fluctuation, PDF at the phase of minimum and maximum κ was shown in Figs. 14(c) and 14(d). In the hydrogen flame, the minimum was around $\theta = 90^\circ$, and the maximum was around $\theta = 270^\circ$. In the methane flame, they were $\theta = 330^\circ$ and $\theta = 150^\circ$, respectively. It can be said that the whole distribution shifts along with the changes in the phase. If none of the fluctuation exists, the distribution should be identical. Therefore, the shift of the whole distribution indicates that the mean flame stretch rate varies during the cycle. The above discussion on Fig. 15 also supports the existence of this fluctuation. Further discussion of the Lewis number effect appears in Sec. III C 3.

C. Results of OH* chemiluminescence imaging

1. Local Rayleigh index map

According to the Rayleigh criterion [46], the local Rayleigh index $\mathrm{RI}_{\mathrm{local}}$ was calculated for each pixel of the instantaneous OH* chemiluminescence image as

$$\mathrm{RI}_{\mathrm{local}} = \frac{1}{T}\int_0^T p'(t)\dot{q}'(t)dt, \tag{8}$$

where, p' is the pressure fluctuation and $\dot{q}'$ is the OH* chemiluminescence intensity fluctuation. The total acquisition time is denoted by T. Note that p' refers to the peak frequency $f_p \pm$ 15 Hz band-pass filtered pressure fluctuation. Figure 16 shows the distribution of the mean OH*

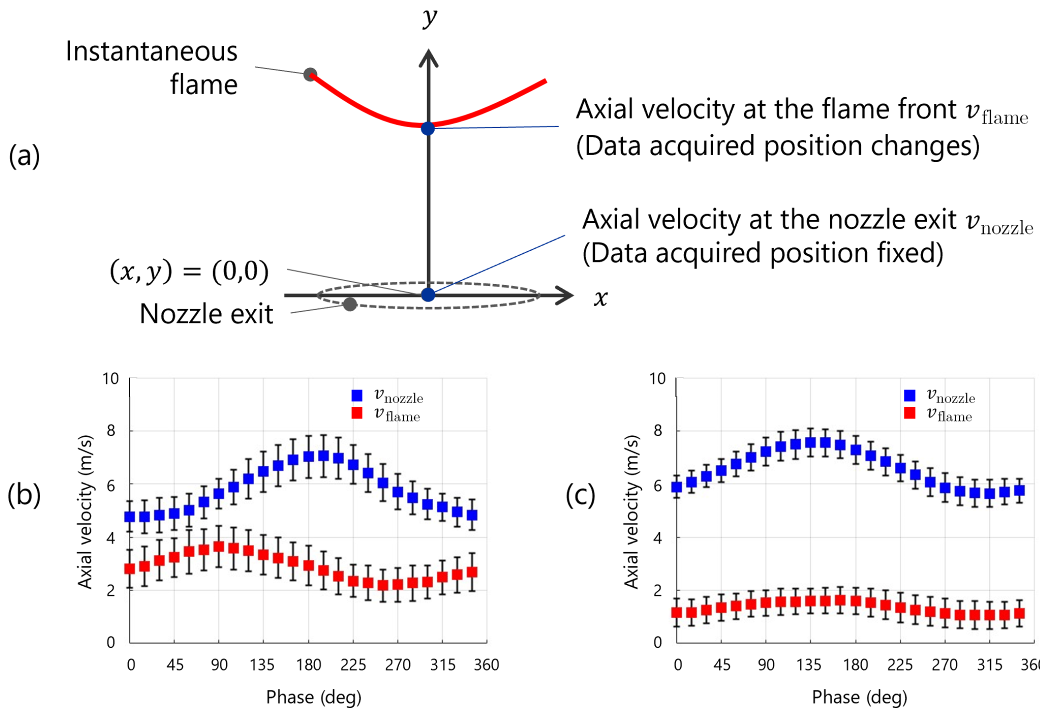

FIG. 15. (a) The schematic of the data acquisition point. The phase-locked averaged axial velocity v_{nozzle} and v_{flame} for (b) hydrogen flame, (c) methane flame. The phase $\theta = 0^\circ$ corresponds to the phase in which the maximum pressure fluctuation amplitude was observed. Blue plot: axial velocity at the nozzle exit v_{nozzle}. Red plot: axial velocity at the flame front v_{flame}.

chemiluminescence intensity and the $\mathrm{RI}_{\mathrm{local}}$ map for each flame. The vertical and horizontal axes are normalized by the inner diameter of the combustor, $D = 35$ mm. Figures 16(a) and 16(b) show the mean OH* chemiluminescence intensity distributions. Figures 16(c) through 16(f) show the local Rayleigh index $\mathrm{RI}_{\mathrm{local}}$ maps. Values are normalized by the maximum $\mathrm{RI}_{\mathrm{local}}$ of each flame. The positive $\mathrm{RI}_{\mathrm{local}}$ expresses the region where the pressure fluctuation and the heat release rate fluctuation are coupled and contribute to the amplification of the thermoacoustic instability. On the other hand, the negative $\mathrm{RI}_{\mathrm{local}}$ indicates the region where pressure fluctuation and the heat release rate fluctuation contribute to decaying the thermoacoustic instability.

According to Figs. 16(c) and 16(d), the heat release rate fluctuation in the swirling flame is coupled with the pressure fluctuation, which is common for both flames. However, the trend at the flame base differs. Here, the flame base is defined as the flame, which is positioned at the region of approximately $-0.3 \leqslant x/D \leqslant 0.3$, $0.2 \leqslant y/D \leqslant 0.5$. Figures 16(e) and 16(f) provide magnified views of the $\mathrm{RI}_{\mathrm{local}}$ map around the flame base along with an enlarged color bar. The average position of the flame front is outlined by a white line. The average position of the flame front is defined by the mean OH* chemiluminescence intensity distributions. It was defined as the pixel, which primarily exceeds 7% of the maximum intensity in each collum in the range of $-0.3 \leqslant x/D \leqslant 0.3$. In the case of the methane flame, $\mathrm{RI}_{\mathrm{local}}$ at the flame base is nearly zero. Conversely, in the hydrogen flame, it is mostly positive along the flame front except in the flame tip along the center axis ($x/D \approx 0$, $y/D \approx 0.2$). These results indicate that in the methane flame, the amplification of the thermoacoustic instability is small at the flame base. In contrast, in the hydrogen flame, the heat release rate fluctuation at the flame base is strongly coupled with the pressure fluctuation. A similar trend was reported by Yilmaz [26], whose investigation of the local Rayleigh index around

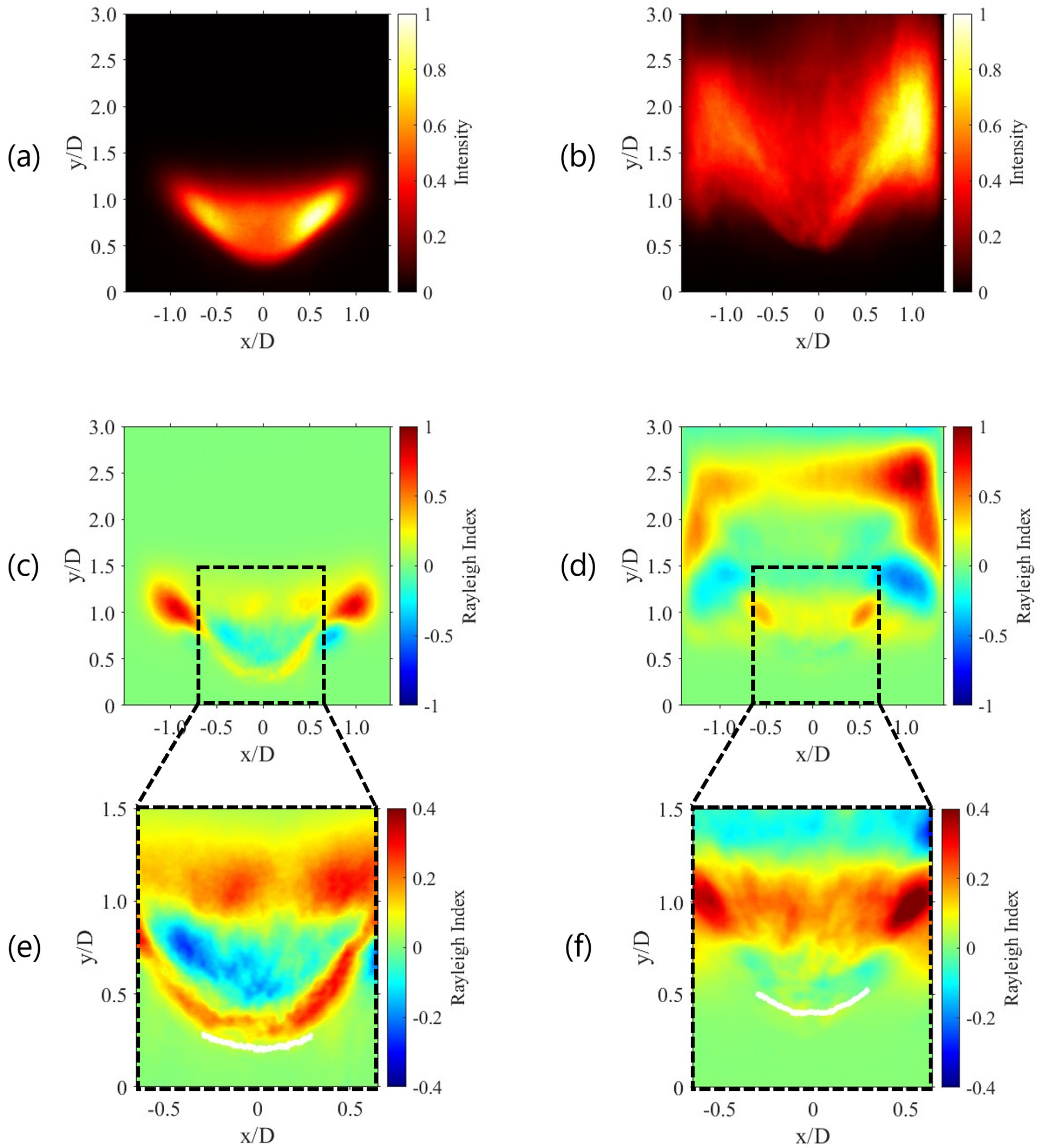

FIG. 16. The mean OH* chemiluminescence intensity distribution for (a) hydrogen flame, (b) methane flame. The local Rayleigh index map for (c) hydrogen flame, (d) methane flame. The magnified image and range of local Rayleigh index map of (c) and (d) with the average flame front determined from the mean OH* chemiluminescence intensity distribution drawn in a white line for (e) hydrogen flame, (f) methane flame.

the flame base revealed that it becomes positive with an increase in the hydrogen composition of the methane/hydrogen mixture fuel.

2. Calculation of chemiluminescence intensity $I_{OH^*,flametip}$

Figure 17 shows an example of the instantaneous OH* chemiluminescence image and a magnified image at the bottom to illustrate the flame tip. The chemiluminescence intensity $I_{\mathrm{OH^*,flametip}}$ was calculated from instantaneous OH* chemiluminescence images. $I_{\mathrm{OH^*,flametip}}$ was defined as the

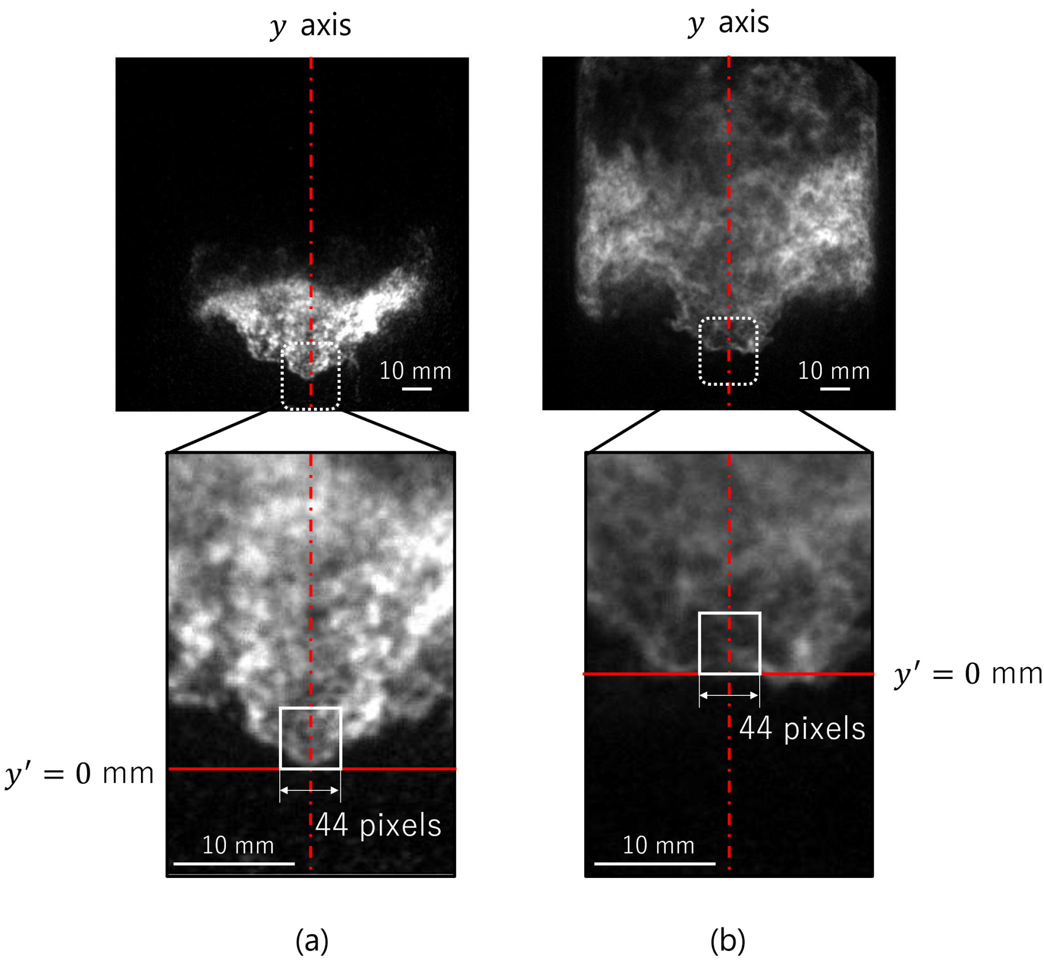

FIG. 17. An example of the instantaneous OH* chemiluminescence image and the concept of the flame tip for (a) hydrogen flame and (b) methane flame. White rectangles represent the area to calculate $I_{\mathrm{OH}^*,\mathrm{flametip}}$. Red lines represent $y' = 0$ mm, which is the intersection point of the estimated flame front and the center axis.

total intensity within the square interrogation window. The interrogation window was set as a 5 mm square, which resulted in a window size of 44 pixels for both flames. This size was determined from the estimated curvature of the flame front; according to Figs. 13(c) and 13(d), the maximum value of the phase-locked averaged curvature R was around 0.1 /mm for both flames, which is equal to 10 mm in curvature radius. Therefore, the window was set to be half of the curvature radius, which was large enough to include the bowl-like shape in the flame tip along the center axis. The bottom of the window was set at $y' = 0$ mm, which is the height of the intersection point of the estimated flame front and the center axis. In Fig. 17, the interrogation window is shown as a white square, and $y' = 0$ mm as a red line.

Then, the chemiluminescence intensity fluctuation $I'_{\mathrm{OH}^*,\mathrm{flametip}}$ was defined as

$$I'_{\mathrm{OH}^*,\mathrm{flametip}} = (I_{\mathrm{OH}^*,\mathrm{flametip}} - \bar{I}_{\mathrm{OH}^*,\mathrm{flametip}})/\bar{I}_{\mathrm{OH}^*,\mathrm{flametip}}, \quad (9)$$

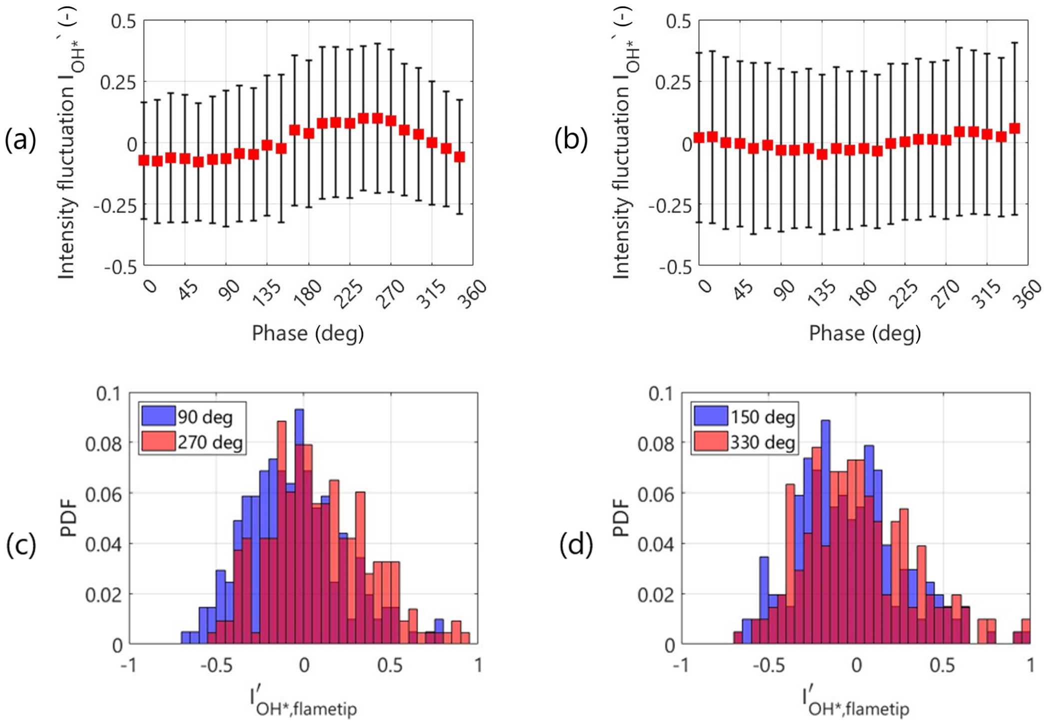

FIG. 18. The phase-locked averaged OH* chemiluminescence intensity fluctuation $I'_{\mathrm{OH*,flametip}}$ for (a) hydrogen flame, (b) methane flame. The phase $\theta = 0^{\circ}$ corresponds to the phase in which the maximum pressure fluctuation amplitude was observed. (c) PDF of $I'_{\mathrm{OH*,flametip}}$ for the hydrogen flame. (d) PDF of $I'_{\mathrm{OH*,flametip}}$ for the methane flame. Phases corresponding to the fluctuation of κ was selected for both flames.

where, $\bar{I}_{\mathrm{OH*,flametip}}$ represents the mean intensity of the entire set of images. In addition, the global chemiluminescence intensity fluctuation $I'_{\mathrm{OH*,global}}$ was defined as

$$I'_{\mathrm{OH*,global}} = (I_{\mathrm{OH*,global}} - \bar{I}_{\mathrm{OH*,global}})/\bar{I}_{\mathrm{OH*,global}}, \tag{10}$$

to allow us to discuss the overall fluctuation during the thermoacoustic instability. $I_{\mathrm{OH*,global}}$ is the summation of all pixels in the field of view. The same phase-locked averaging analysis [45] was performed for $I'_{\mathrm{OH*,flametip}}$ and $I'_{\mathrm{OH*,global}}$ to discuss the periodic fluctuation during the thermoacoustic instability. Details of the phase-locked analysis were described in Sec. III B 3. A total of 5000 OH* chemiluminescence images were acquired, and approximately 200 images were assigned to each phase.

3. Phase-locked averaged $I'_{OH*,flametip}$ and $I'_{OH*,global}$, and the Lewis number effect during the thermoacoustic instability

Figures 18(a) and 18(b) show the phase-locked averaged OH* chemiluminescence intensity fluctuation $I'_{\mathrm{OH*,flametip}}$. The error bar denotes the standard deviation. To further discuss the fluctuation, PDF was shown in Figs. 18(c) and 18(d). Phases were selected as same as Fig. 14, which are $\theta = 90^{\circ}$ and $\theta = 270^{\circ}$ in the hydrogen flame, and $\theta = 330^{\circ}$ and $\theta = 150^{\circ}$ in the methane flame. In the hydrogen flame, the whole distribution slightly changes. Specifically, the center of the distribution crosses 0. On the other hand, in the methane flame, the distribution is nearly identical. This suggests that in the methane flame, a fluctuation is too weak to be observed during the cycle.

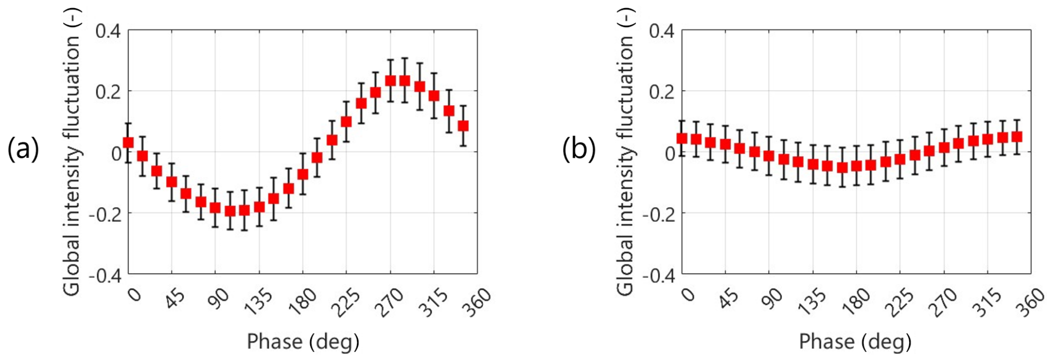

FIG. 19. The phase-locked averaged global OH* chemiluminescence intensity fluctuation $I'_{\mathrm{OH*,global}}$ for (a) hydrogen flame, (b) methane flame. The phase $\theta = 0^\circ$ corresponds to the phase in which the maximum pressure fluctuation amplitude was observed.

According to Fig. 18, in the hydrogen flame, a periodic fluctuation of $I'_{\mathrm{OH*,flametip}}$ corresponds to the fluctuation of the flame stretch rate κ as shown in Fig. 14(a). Because the Lewis number of the hydrogen-air premixture is $\mathrm{Le} = 0.34 < 1$, the hydrogen flame exhibited high sensitivity to the flame stretch rate κ fluctuations, resulting in the intensity $I'_{\mathrm{OH*,flametip}}$ fluctuations. These results indicate a strong correlation between κ and $I'_{\mathrm{OH*,flametip}}$, implying that the Lewis number effect occurred in the hydrogen flame even during the thermoacoustic instability. In contrast, such a correlation was not observed in the methane flame; According to Fig. 14(b), the flame stretch rate κ also had a periodic fluctuation within the range of 303–407 /s. However, no synchronizing fluctuation with the flame stretch rate κ was observed in the OH* chemiluminescence intensity fluctuation $I'_{\mathrm{OH*,flametip}}$. Since the Lewis number of the methane-air premixture is $\mathrm{Le} = 0.97 \approx 1$, the methane flame had low sensitivity to the flame stretch rate κ fluctuation. This indicates a weak correlation between κ and $I'_{\mathrm{OH*,flametip}}$. The following analysis on the flame tip further indicates that the hydrogen flame is more sensitive to the flow fluctuation than the methane flame.

Figure 19 shows the phase-locked averaged global OH* chemiluminescence intensity fluctuation $I'_{\mathrm{OH*,global}}$. It is evident that the hydrogen flame exhibits approximately three times larger fluctuation, which corresponds to the larger pressure fluctuation amplitude. Given that $\theta = 0^\circ$ or 360° is defined as the phase in which the maximum pressure amplitude occurs, it is possible to evaluate whether the pressure fluctuation and the heat release rate fluctuation satisfy the necessary condition for amplifying the thermoacoustic instability. This is determined by the phase difference between the pressure fluctuation and $I'_{\mathrm{OH*,global}}$ or $I'_{\mathrm{OH*,flametip}}$. When the phase difference is below 90° (i.e., in-phase), this indicates that the pressure fluctuation and $I'_{\mathrm{OH*,global}}$ or $I'_{\mathrm{OH*,flametip}}$ is coupled to amplify the thermoacoustic instability.

As for the hydrogen flame, according to Fig. 19(a), the phase difference between the pressure fluctuation and $I'_{\mathrm{OH*,global}}$ is 75°, indicating that it is in-phase. However, as shown in Fig. 18(a), the phase difference between the pressure fluctuation and $I'_{\mathrm{OH*,flametip}}$ is 90°–120°, which is possibly out of phase. This means that the heat release rate fluctuation at the flame tip weakly contributes to amplifying the thermoacoustic instability. A review of Fig. 16(e) shows that in the hydrogen flame, the local Rayleigh index $\mathrm{RI}_{\mathrm{local}}$ at the flame tip was nearly 0; this region partially matches the interrogation window for calculating $I'_{\mathrm{OH*,flametip}}$. In other words, the of the positive feedback of pressure and heat release fluctuations did not occur at the flame tip, where the local Lewis number effect was observed. Comparing Figs. 18(a) and 19(a), there is a phase difference of 45° between $I'_{\mathrm{OH*,flametip}}$ and $I'_{\mathrm{OH*,global}}$. This phase difference is at least not caused by the convection of the flow because there is not sufficient time for propagation from the flame tip along the center axis to the downstream of the flame within an interval of 45° $(1/285\ [\mathrm{Hz}] \times\ 1/8 \approx 0.00044\ \mathrm{s})$.

On the other hand, in the methane flame, no synchronization is confirmed between $I'_{OH^*,flametip}$ and $I'_{OH^*,global}$ as shown in Figs. 18(b) and 19(b). It is conjectured that the pronounced coupling is observed exclusively in the swirling flame of the methane flame. The local Rayleigh index map shown in Fig. 16(f) also supports the discussion; RI_{local} was nearly 0 at the flame base which indicates that the coupling of the pressure fluctuation and the heat release rate fluctuation is weak. According to Fig. 19(b), the phase difference between the pressure fluctuation and $I'_{OH^*,global}$ is 15° and it is in phase. Further investigation is needed to determine why the phase difference between the pressure fluctuation and $I'_{OH^*,global}$ varies between the hydrogen flame and the methane flame.

As mentioned in Sec. I, the relation between the Lewis number effect and the thermoacoustic instability has been discussed previously by examining the global characteristics such as the pressure amplitude or the global heat release rate fluctuations. This is because thermoacoustic instability involves global fluctuations in the flow field and flame characteristics. However, this study has revealed the existence of the Lewis number effect in the local flame front, i.e., the flame tip in the vicinity of the center axis. Specifically, in the hydrogen flame, the Lewis number effect may lead to a strong relationship between the local flow and the intensity fluctuations (i.e., heat release rate fluctuations). Conversely, in the methane flame, the contribution of the Lewis number effect is weak. The improved understanding of the local flame-flow interaction in the current study is significant for elucidating the detailed physics behind the thermoacoustic instability.

However, clarifying how the local Lewis number effect influences the global flame-flow interaction and drives the thermoacoustic instability is out of the scope of the current study. This should be discussed in the next study to gain a deeper understanding. Also, it must be noted that the two flames cannot be compared merely by the Lewis number effect. For example, a damping effect, such as heat loss from the combustor wall, must be considered. As represented in Fig. 16(b), the methane flame is distributed widely and is expected to touch the chamber wall, which can cause heat loss.

IV. CONCLUSIONS

Thermoacoustic instabilities were observed in the hydrogen-air flame ($\phi = 0.28$) and the methane-air flame ($\phi = 0.62$) stabilized in a low-swirl combustor whose geometric swirl number was 0.39. Pressure fluctuation measurements p', the OH* chemiluminescence imaging q', and PIV v' were performed simultaneously. The hydrogen flame exhibited a pressure fluctuation amplitude nearly three times larger than that of the methane flame. During the thermoacoustic instability, a significant difference in the local Rayleigh index at the flame base was confirmed between the hydrogen flame and the methane flame. The flame-flow interaction in the hydrogen flame was assessed by examining the impact of the Lewis number effect in comparison to the methane flame. This study aimed to clarify the Lewis number effect on the local flame-flow interaction during the thermoacoustic instability, unlike previous studies which have mainly focused on the comparison of the pressure amplitude and the global heat release rate. Thereby, the flame stretch rate κ and the OH* chemiluminescence intensity fluctuation at the flame tip along the center axis $I'_{OH^*,flametip}$ were calculated. To assist the discussion, a Rayleigh index analysis was also conducted. The following results were obtained.

In both the hydrogen flame and the methane flame, a periodic fluctuation of the flame stretch rate κ was confirmed at the flame tip. In the methane flame, since the Lewis number of the premixture is near unity ($Le = 0.97$), the flame exhibited low sensitivity to the fluctuation of the flame stretch rate κ, resulting in a weak correlation between the flame stretch rate κ and the OH* chemiluminescence intensity $I'_{OH^*,flametip}$. On the other hand, in the hydrogen flame, since the Lewis number of the premixture is below unity ($Le = 0.34$), $I'_{OH^*,flametip}$ synchronized with the fluctuation of κ, resulting in a strong correlation between κ and $I'_{OH^*,flametip}$. These results indicated that in the hydrogen flame, the Lewis number effect is observable, and there exists a tight interaction between the flow fluctuation and the heat release rate fluctuation in the local flame tip.

According to the local Rayleigh index analysis, the results differed for the two flame bases. In the methane flame, the local Rayleigh index was nearly 0, which indicated that the flame base has small contribution to amplify the thermoacoustic instability. In the hydrogen flame, the local Rayleigh index was positive at the flame base except at the flame tip along the center axis, which was nearly 0. This indicated that in the hydrogen flame, the pressure fluctuation and the heat release rate fluctuation is strongly coupled at the flame base. Meanwhile, at the flame tip, where the Lewis number effect was observed in the current study, the positive feedback of the pressure and the heat release rate fluctuations did not occur.

It remains as a challenge to clarify how the local Lewis number effect influences the global thermoacoustic instability. Further research is needed for a comprehensive comparison of both flames.

ACKNOWLEDGMENTS

The authors thank Kentaro Horikawa of Keio University for assistance during data collection. This work was supported by JSPS KAKENHI Grants No. JP19H02076 and No. JP22H00192.

[1] A. Wulff and J. Hourmouziadis, Technology review of aeroengine pollutant emissions, Aerosp. Sci. Technol. **1**, 557 (1997).

[2] A. A. Peracchio and W. M. Proscia, Nonlinear heat-release/acoustic model for thermoacoustic instability in lean premixed combustors, J. Eng. Gas Turbine Power **121**, 415 (1999).

[3] M. Stöhr, I. Boxx, C. Carter, and W. Meier, Dynamics of lean blowout of a swirl-stabilized flame in a gas turbine model combustor, Proc. Combust. Inst. **33**, 2953 (2011).

[4] J. Fritz, M. Kröner, and T. Sattelmayer, Flashback in a swirl burner with cylindrical premixing zone, J. Eng. Gas Turbine Power **126**, 276 (2004).

[5] T. Lieuwen and V. Yang, *Combustion Instabilities in Gas Turbine Engines* (American Institute of Aeronautics and Astronautics, Portland, 2005), p. 10.

[6] M. K. Kim, J. Yoon, S. Park, M. C. Lee, and Y. Yoon, Effects of unstable flame structure and recirculation zones in a swirl-stabilized dump combustor, Appl. Therm. Eng. **58**, 125 (2013).

[7] J. P. Moeck, J. F. Bourgouin, D. Durox, T. Schuller, and S. Candel, Nonlinear interaction between a precessing vortex core and acoustic oscillations in a turbulent swirling flame, Combust. Flame **159**, 2650 (2012).

[8] H. Zhao, G. Li, D. Zhao, Z. Zhang, D. Sun, W. Yang, S. Li, Z. Lu, and Y. Zheng, Experimental study of equivalence ratio and fuel flow rate effects on nonlinear thermoacoustic instability in a swirl combustor, Appl. Energy **208**, 123 (2017).

[9] S. S. Rashwan, A. Mohany, and I. Dincer, Investigation of self-induced thermoacoustic instabilities in gas turbine combustors, Energy **190**, 116362 (2020).

[10] D. Beerer, V. McDonell, P. Therkelsen, and R. K. Cheng, Flashback and turbulent flame speed measurements in hydrogen/methane flames stabilized by a low-swirl injector at elevated pressures and temperatures, J. Eng. Gas Turbine Power **136**, 031502 (2014).

[11] T. Sattelmayer, C. Mayer, and J. Sangl, Interaction of flame flashback mechanisms in premixed hydrogen-air swirl flames, J. Eng. Gas Turbine Power **138**, 011503 (2016).

[12] T. Shoji, S. Tachibana, T. Suzuki, Y. Nakazumi, and T. Yokomori, A new pattern of flame/flow dynamics for lean-premixed low-swirl hydrogen turbulent jet flames under thermoacoustic instability, Proc. Combust. Inst. **38**, 2835 (2021).

[13] S. J. Shanbhogue, Y. S. Sanusi, S. Taamallah, M. A. Habib, E. M. A. Mokheimer, and A. F. Ghoniem, Flame macrostructures, combustion instability and extinction strain scaling in swirl-stabilized premixed CH_4/H_2 combustion, Combust. Flame **163**, 494 (2016).

[14] M. Wang, Y. Zhong, and K. Deng, Experiment investigation of the effects of hydrogen content on the combustion instability of methane/hydrogen lean premixed swirl flames under different acoustic frequency ranges, AIP Adv. **9**, 045206 (2019).
[15] S. Joo, S. Kwak, J. Lee, and Y. Yoon, Thermoacoustic instability and flame transfer function in a lean direct injection model gas turbine combustor, Aerosp. Sci. Technol. **116**, 106872 (2021).
[16] G. Oztarlik, L. Selle, T. Poinsot, and T. Schuller, Suppression of instabilities of swirled premixed flames with minimal secondary hydrogen injection, Combust. Flames **214**, 266 (2020).
[17] A. Kushwaha, P. Kasthuri, S. A. Pawar, R. I. Sujith, I. Chterev, and I. Boxx, Dynamical characterization of thermoacoustic oscillations in a hydrogen-enriched partially premixed swirl stabilized methane/air combustor, J. Eng. Gas Turbine Power **143**, 121022 (2021).
[18] A. Datta, S. Gupta, I. Cheterv, I. Boxx, and S. Hemchandra, Impact of hydrogen addition on the thermoacoustic instability and precessing vortex core dynamics in a CH_4/H_2/air technically premixed combustor, J. Eng. Gas Turbine Power **144**, 021013 (2022).
[19] J. G. Aguilar, E. Æsøy, and J. D. Dawson, The influence of hydrogen on the stability of a perfectly premixed combustor, Combust. Flames **245**, 112323 (2022).
[20] B. Ahn, T. Indlekofer, J. R. Dawson, and N. A. Worth, Heat release rate response of azimuthal thermoacoustic instabilities in a pressurized annular combustor with methane/hydrogen flames, Combust. Flames **244**, 112274 (2022).
[21] D. Ebi and N. T. Clemens, Experimental investigation of upstream flame propagation during boundary layer flashback of swirl flames, Combust. Flame **168**, 39 (2016).
[22] C. K. Chan, K. S. Lau, W. K. Chin, and R. K. Cheng, Freely propagating open premixed turbulent flames stabilized by swirl, Symp. Combust. Proc. **24**, 511 (1992).
[23] R. K. Cheng, D. Littlejohn, P. A. Strakey, and T. Sidwell, Laboratory investigations of a low-swirl injector with H_2 and CH_4 at gas turbine conditions, Proc. Combust. Inst. **32**, 3001 (2009).
[24] S. Tachibana, K. Kanai, S. Yoshida, K. Suzuki, and T. Sato, Combined effect of spatial and temporal variations of equivalence ratio on combustion instability in a low-swirl combustor, Proc. Combust. Inst. **35**, 3299 (2015).
[25] Z. Cao, Y. Xiao, W. Song, and W. Li, Experimental study on thermoacoustic instability and emission characteristics of premixed swirl flame in a longitudinal combustor, Int. J. Therm. Sci. **172**, 107354 (2022).
[26] I. Yilmaz, A. Ratner, M. Ilbas, and Y. Huang, Experimental investigation of thermoacoustic coupling using blended hydrogen-methane fuels in a low swirl burner, Int. J. Hydrog. Energy **35**, 329 (2010).
[27] P. L. Therkelsen, Self-Induced Unstable Behaviors of CH_4 and H_2/CH_4 flames in a model combustor with a low-swirl injector, Combust. Flame **160**, 304 (2013).
[28] F. Li, X. Tian, M. Du, L. Shi, and J. Cui, Effects of intrinsic flame instabilities on thermoacoustic oscillations in lean premixed gas turbines, J. Eng. Gas Turbine Power **144**, 051007 (2022).
[29] S. H. Yoon, T. J. Noh, and O. Fujita, Effects of lewis number on generation of primary acoustic instability in downward-propagating flames, Proc. Combust. Inst. **36**, 1603 (2017).
[30] Chung. K. Law, *Combustion Physics* (Cambridge University Press, New York, 2006), p. 146.
[31] E. Abbasi-Atibeh, S. Jella, and J. M. Bergthorson, Fuel variation effects in propagation and stabilization of turbulent counter-flow premixed flames, J. Eng. Gas Turbine Power **141**, 031024 (2019).
[32] F. H. Vance, Ç. Alanyalıoğlu, and C. Hasse, Analysis of lewis number effects on dynamic response of laminar premixed flames, Combust. Flame **248**, 112508 (2023).
[33] S. D. Salusbury and J. M. Bergthorson, Maximum stretched flame speeds of laminar premixed counter-flow flames at variable lewis number, Combust. Flame **162**, 3324 (2015).
[34] X. Cai, J. Wang, Z. Bian, H. Zhao, M. Zhang, and Z. Huang, Self-similar propagation and turbulent burning velocity of CH_4/H_2/air expanding flames: Effect of lewis number, Combust. Flame **212**, 1 (2020).
[35] R. K. Cheng, D. T. Yegian, M. M. Miyasato, G. S. Samuelsen, C. E. Benson, R. Pellizzari, and P. Loftus, Scaling and development of low-swirl burners for low-emission furnaces and boilers, Proc. Combust. Inst. **28**, 1305 (2000).
[36] Y. Liu, J. Tan, H. Wang, and L. Lv, Characterization of heat release rate by OH* and CH* chemiluminescence, Acta Astronaut. **154**, 44 (2019).

[37] A. K. Prasad and K. Jensen, Scheimpfulg stereocamera for particle image velocimetry in liquid flows, Appl. Opt. **34**, 7092 (1995).
[38] S. Taamallah, Z. A. Labry, S. J. Shanbhogue, and A. F. Ghoniem, Thermo-acoustic instabilities in lean premixed swirl-stabilized combustion and their link to acoustically coupled and decoupled flame macrostructures, Proc. Combust. Inst. **35**, 3273 (2015).
[39] R. M. Gejji, C. Huang, C. Fugger, C. Yoon, and W. Anderson, Parametric investigation of combustion instabilities in a single-element lean direct injection combustor, Int. J. Spray and Combust. Dyn. **11**, 1 (2018).
[40] N. Balasubramanian, D. Cao, I. Greenberg, and D. Michaels, Mitigation of combustion instabilities by local diluent injection in a premixed swirl stabilized combustor, Combust. Flame **245**, 112334 (2022).
[41] Y. Zheng, L. Weller, and S. Hochgreb, Instantaneous flame front identification by mie scattering vs. OH PLIF in low turbulence bunsen flame, Exp. Fluids **63**, 79 (2022).
[42] F. A. Williams, A review of some theretical consideration of turbulent structure, AGARD Conf. Proc. **164**, II1-1 (1975).
[43] S. H. Chung and C. K. Law, An invariant derivation of flame stretch, Combust. Flame **55**, 123 (1984).
[44] R. K. Cheng, D. Littlejohn, W. A. Nazeer, and K. O. Smith, Laboratory studies of the flow field characteristics of low-swirl injectors for adaptation to fuel-flexible turbines, J. Eng. Gas Turbine Power **130**, 021501 (2008).
[45] F. Ostermann, R. Woszidlo, C. N. Nayeri, and C. O. Paschereit, Phase-averaging methods for the natural flowfield of a fluidic oscillator, AIAA J. **53**, 2359 (2015).
[46] L. Rayleigh, The explanation of certain acoustical phenomena, Nature (London) **18**, 319 (1878).